14th International Symposium on Turbulence and Shear Flow Phenomena (TSFP14)
Heidelberg, Germany, July 28–31, 2025

TURBULENCE STATISTICS IN A BOUNDARY LAYER OF A CONTROLLED DIFFUSION AIRFOIL AIRFOIL AT HIGH ANGLE-OF-ATTACK

Ziyang Zhou
Mechanical Engineering Department
Université de Sherbrooke
Sherbrooke, Quebéc, J1K2R1, Canada
zhou.ziyang@usherbrooke.ca

Stéphane Moreau
Mechanical Engineering Department
Université de Sherbrooke
Sherbrooke, Quebéc, J1K2R1, Canada
stephane.moreau@usherbrooke.ca

Marlène Sanjosé
Aerospace Engineering Department
École de technologie supérieure
Montréal, QC, H3C 1K3 Canada
marlene.sanjose@etsmtl.ca

ABSTRACT

A direct numerical simulation (DNS) of a controlled diffusion (CD) airfoil at $Re = 150{,}000$, $M = 0.2$, and $\alpha = 15^\circ$ has been performed with the PowerFLOW Lattice Boltzmann Method (LBM) solver which showed velocity profiles which scaled well with embedded shear layer scaling. The strong anisotropy typically seen in attached flow cases due to long streamwise coherent structures diminished from $\alpha = 8^\circ$ to $\alpha = 15^\circ$. Strong spanwise coherence near the middle of the boundary layer was present at $\alpha = 15^\circ$ and not at $\alpha = 8^\circ$ due to Kelvin Helmholtz rollers in the former case.

Introduction

The prediction of fan noise is instrumental to the design of measures to reduce them. Among several noise sources, trailing edge noise is significant because it represents the minimum achievable noise level at design conditions. This is especially relevant in wind turbines and low speed fans such (Sanjosé & Moreau, 2018) where trailing edge noise represents the main contributor at higher frequencies beyond 4 kHz (Lee *et al.*, 2021). Although large eddy simulations (LES) (Zhu *et al.*, 2018) are able to capture the broadband spectrum of farfield noise generated by these rotating machines, they are computationally expensive for design studies.

To approach this problem, Amiet's model (Amiet, 1975; Roger & Moreau, 2005) can be used to yield trailing edge noise caused by the turbulent boundary layer for stationary airfoil in subsonic flows with speed and accuracy. Subsequently, by approximating rotating blades as a stack of airfoils in rectilinear motion, trailing edge noise from rotating blades may be obtained. Yet, the model requires the prediction of the wall pressure spectra (WPS), ϕ_{pp}, near the airfoil trailing edge.

On the one hand, semi-empirical models (Lee *et al.*, 2021; Pargal, 2023) use boundary layer parameters that can be obtained from RANS simulations to predict WPS beneath the boundary layer. However, these models contain constants that are empirically obtained from a limited number of experiments. Furthermore, most semi-empirical models that use the wall shear stress τ_w break down in separated flows.

On the other hand, an analytical approach also exists to yield ϕ_{pp} by considering the Poisson equation, which governs the pressure fluctuations in a turbulent boundary layer. Solving this equation with appropriate boundary conditions (see (Grasso *et al.*, 2019)) yields the pressure fluctuation at the wall. Neglecting the turbulence-turbulence interaction term (Kraichnan, 1956), and assuming that all mean velocity gradients except $\frac{\partial U_1(X_3)}{x_3}$ are negligible, the wall-pressure spectrum $\phi_{pp}(\omega)$ can be related to the two-wavenumber spectrum expressed in body-fitted airfoil coordinates representing the streamwise (x_1), spanwise (x_2), and wall-normal (x_3) directions:

$$\Phi_{pp}(k_1,k_2) = 4\rho_0^2 \iint_0^\infty \frac{k_1^2}{k^2} e^{-(X_3+X_3')k} \frac{\partial U_1(X_3)}{x_3} \frac{\partial U_1(X_3')}{x_3} \times \phi_{33}\, dX_3 dX_3' \quad (1)$$

where ϕ_{33} is the vertical velocity fluctuation cross-spectral density defined as:

$$\phi_{33}(k_1,k_2,r_3) = \frac{\sqrt{u_3(\bar{X}_3)^2\, u_3(\bar{X}_3')^2}}{4\pi} \iint_{-\infty}^{\infty} R_{33}(r_1,r_2,r_3) \times \cos(k_1 r_1)\cos(k_2 r_2)\, dr_1 dr_2 \quad (2)$$

To correctly model the source term in this formulation, the velocity correlation function function (R_{33}) is needed. To obtain this, both the integral length scale, Λ, and the anisotropic factor, α_j, are required (see equations (2.16) and (2.22) in (Panton & Linebarger, 1974)). In the present work, a DNS is conducted of the CD airfoil at $\alpha = 15^\circ$ to enable the characterization of R_{33} and anisotropy for an APG regime with separated flow. The results of this simulation are compared to the DNS setup of an $\alpha = 8^\circ$ CD airfoil from (Zhou *et al.*, 2025) with increased voxel refinement.

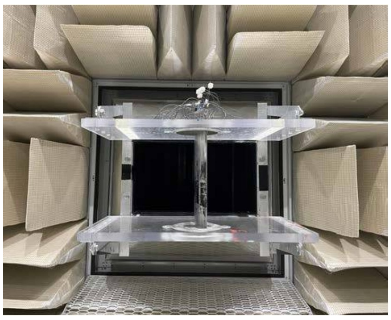

Figure 1. Experimental setup showing an instrumented airfoil in the UdeS anechoic open-jet facility.

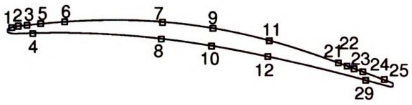

Figure 2. RMP location on the CD airfoil.

1 Numerical setup

1.1 Computational Domain

The computational domain in this simulation corresponds to several open-jet experimental set-ups (Jaiswal *et al.*, 2020) including that in the anechoic wind tunnel facility at Université de Sherbrooke (UdeS) shown in Fig. 1. The CD airfoil is placed in the potential core of the jet. The airfoil chord length of the airfoil is 0.1356 m. The inlet velocity is 16 m/s with a small coflow of 0.165 m/s. 21 Remote Microphone Probes (RMP) are flush mounted on various locations on the midspan of the CD airfoil mock-up to measure mean and fluctuating wall pressures as shown in Fig. 2. Boundary conditions are set as shown in Fig. 3. Note that including the installation effects are absolutely necessary to reproduce the proper loading on the airfoil and thus the proper turbulent boundary layer development on the suction side and consequently the noise radiated in the far field (Moreau *et al.*, 2003).

The choice of span width is $0.1c$ for $\alpha = 8°$ (Jaiswal *et al.*, 2020). It has been increased to $0.36c$, as it has already been shown experimentally (Jaiswal *et al.*, 2023) that the spanwise coherence length of the surface pressure of a CD airfoil at a geometrical angle of attack of $\alpha = 15°$ is less than $0.36c$ (which is 3.6 times larger than in the previous LES case (Christophe *et al.*, 2009)).

1.2 Numerical method

In the present study, the LBM (He & Luo, 1997; Chen, 1998) is applied to the CD airfoil in the full wind-tunnel configuration to account for the effect of the jet on the airfoil loading (Moreau *et al.*, 2003; Zhou *et al.*, 2025). The LBM (from the PowerFlow V6-2024-R1 solver) is naturally transient and compressible, leading to an insight on hydrodynamics mechanisms responsible for TE noise sources. In LBM, the Boltzmann equation is solved on a lattice in order to obtain the discrete-velocity distribution function in the multi-dimensional phase space, $f_i(\mathbf{x}, \mathbf{c}, t)$, where $\mathbf{x}$ is the particle position, $\mathbf{c}$ is the particle velocity and t is time. For the low speed conditions examined in this study, the classical D3Q19 lattice is used, which means that the three dimensional isothermal flow field is solved using 19 directions in-phase space. The classical BGK relaxation model is used for the collision operator. To obtain density ρ and momentum ρu, weighted sums of f_i are calculated (Krüger *et al.*, 2017) by $\rho(\mathbf{x},t) = \sum_i f_i(\mathbf{x}, c_i, t)$ and $\rho u(\mathbf{x},t) = \sum_i c_i f_i(\mathbf{x}, c_i, t)$. All computations were conducted on 1536 AMD EPYC 9655 cores at 2.6 GHz.

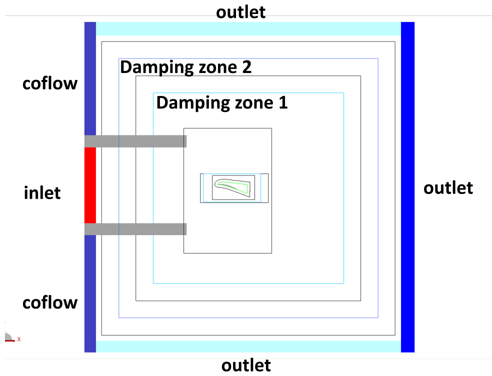

Figure 3. Computational domain with VR regions.

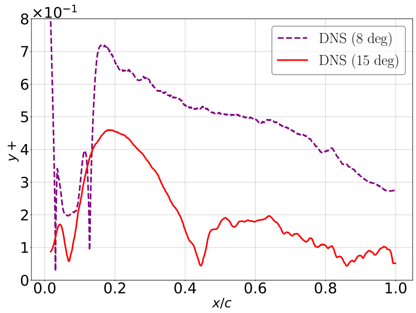

Figure 4. y^+ over suction surface of the CD airfoil.

2 Mesh Resolution

In order to resolve smaller flow structures, voxel regions (VR) are defined in which the voxel size Δx is specified. 8 voxel regions, shown by the black and green lines in Fig. 3, are used in the computational domain. The voxel regions are used to impose the required y^+ on the surface of the airfoil and transition to larger cell sizes in areas further away. A voxel size of 0.0592 mm is used in the finest VR region shown by green lines in Fig 3 of the present $\alpha = 15°$ case and this is 4 times the finest voxel size of the $\alpha = 8°$ case in (Zhou *et al.*, 2025). Despite this, as seen in Fig 4, $y^+ < 1.0$ is achieved over most of the airfoil surface since velocity gradients are not as high near the wall. A balance of turbulence kinetic energy (TKE) is performed on the $\alpha = 8°$ case to verify a sufficient grid resolution. Note that to achieve such a balance in a LBM framework, all gradients need to be evaluated from the reconstructed conservative variables interpolated on a body-fitted curvilinear grid. The latter interpolation uses a high-order Lagrange interpolation scheme as described in (Deuse & Sandberg, 2020). Fig 5 shows this TKE balance at RMP7 in the zero-pressure gradient region. As expected, turbulence production increases away from the wall and peaks at $y^+ = 10$ where it exceeds the dissipation term. When moving toward the trailing edge in the adverse pressure gradient region, the strength of the inner layer peak increases and moves toward the wall. In both regions, the

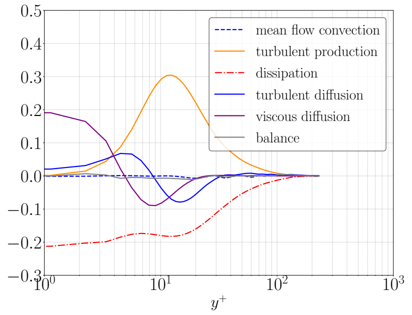

Figure 5. Turbulence kinetic energy balance at $\alpha = 8°$ at RMP7.

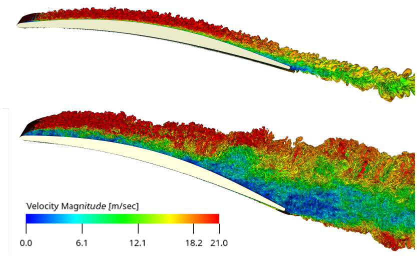

Figure 6. $\lambda_2 = -1.0$ of CD airfoil for $\alpha = 8°$ (above) and $\alpha = 15°$ (below).

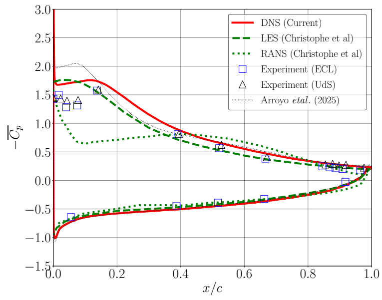

Figure 7. Mean pressure coefficient.

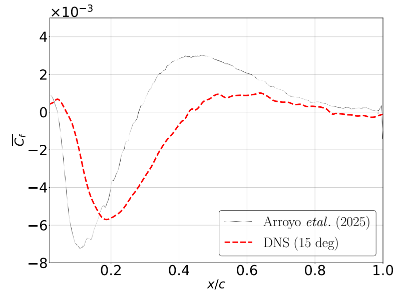

Figure 8. Mean friction coefficient.

balance term is close to zero, which shows adequate grid resolution to resolve the dissipation term throughout the boundary layer.

3 Results and Discussion

3.1 Instantaneous flow

The instantaneous flow topology, shown using the λ_2 criterion in Fig. 6, reveals much larger separation zones in $\alpha = 15°$ than at $\alpha = 8°$. For $\alpha = 15°$, the boundary layer separates first at the leading edge, forming an laminar separation bubble (LSB) and then undergoes laminar-to-turbulent transition via Kelvin-Helmholtz instabilities before reattachment near the mid chord. Near the trailing edge, large spanwise coherent structures as seen in (Jaiswal *et al.*, 2023) are shed.

3.2 Mean flow

The mean pressure coefficient, defined as $C_p = (\overline{p} - p_{ref})/0.5\rho U_\infty^2$, shows good agreement with the LES of (Christophe *et al.*, 2009) and the DNS of (Arroyo Ramo *et al.*, 2026) for $x/c > 0.4$. The extent of the separated shear layer near the leading edge likely explains the differences in C_p for $0 < x/c < 0.4$ between the current simulation and that of (Arroyo Ramo *et al.*, 2026). In the present simulation, the nozzle lips are included to capture confinement effects, allowing the shear layer from the nozzle to develop naturally. In contrast, (Arroyo Ramo *et al.*, 2026) modelled the shear layer via fixed boundary conditions, leading to different confinement effects on the airfoil. This difference causes a discrepancy in the mean size of the separation zone. The zones of flow separation over the airfoil suction surface are revealed using the friction coefficient, $C_f = \overline{\tau_w}/0.5\,\rho\,U_\infty^2$, shown in Fig. 8. The separation zone extends for 40% of the airfoil before reattaching at $x/c = 0.5$ and the flow separates again at $x/c = 0.9$. The profiles of the mean tangential velocity U_t normalized by outer scales are given in Fig. 9. The outer scaling proposed by (Wei & Knopp, 2023) is found to collapse the flow profile well away from the wall and the results matched the empirical fit given by

$$\frac{U_e - U_t}{U_e - U_m} = 1 - \mathrm{erf}\left(1.3y^* + 0.21(1.3y^*)^4\right) \quad (3)$$

where U_m is the tangential velocity at location of max $|\overline{uv}|$, $y^* = \frac{y - y_m}{\delta_e - y_m}$ and y_m is the wall normal location of max $|\overline{uv}|$. According to (Wei & Knopp, 2023), this level of agreement hints at a similarity between the outer layer and free shear turbulent flows. It also signals a level of decoupling (see (Devenport & Lowe, 2022)) of the outer layer from the inner layer and the influence of the wall.

3.3 Boundary layer parameters

In order to shed light on the mean flow field in the present configurations, the boundary layer thickness δ is given in Fig. 10 along with displacement thickness δ^*, momentum thickness θ and the Clauser parameter β_{δ^*}. Note that δ is defined here in the same way as in (Caiazzo *et al.*, 2023), using the criterion of 95% total pressure recovery. Meanwhile, the Clauser parameter, $\beta_{\delta^*} = \delta^*/q\frac{dp}{ds}$ is given in terms of dynamic pressure q and boundary-layer thickness δ^*.

Fig. 10, shows that the current DNS sees a faster growth of boundary layer thickness than in (Arroyo Ramo *et al.*, 2026). This is likely to also be a result of difference in confinement as larger variations of incidence are allowed in the present DNS. Moreover, because of the consistently higher values of β_{δ^*}, the growth of the boundary-layer thicknesses in the $\alpha = 15°$ cases is much more dramatic than that in the $\alpha = 8°$ case. Meanwhile, the experiment on the CD airfoil at $\alpha = 15°$ in an open jet wind tunnel by (Jaiswal *et al.*, 2023) gives a boundary layer thickness closer to the current DNS

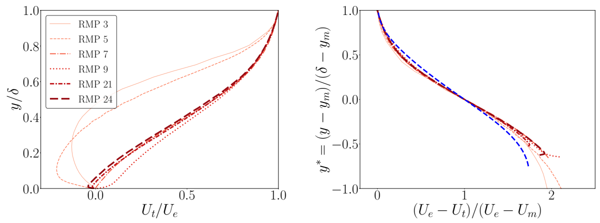

Figure 9. Mean velocity profile normalized by U_e (left) and $U_e - U_m$ (right). Lines of increasing thickness signify location further downstream. Profiles taken at RMP 3, 5, 7, 9, 21 and 24 at $\alpha = 15°$. Blue line is Eq. (3).

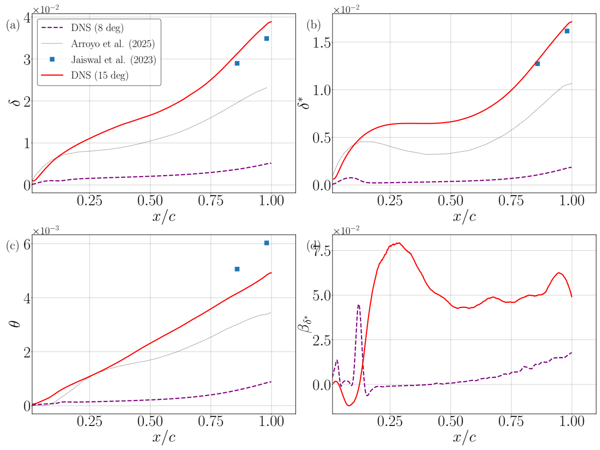

Figure 10. δ, δ^*, θ and β_{δ^*} over suction surface of the CD airfoil.

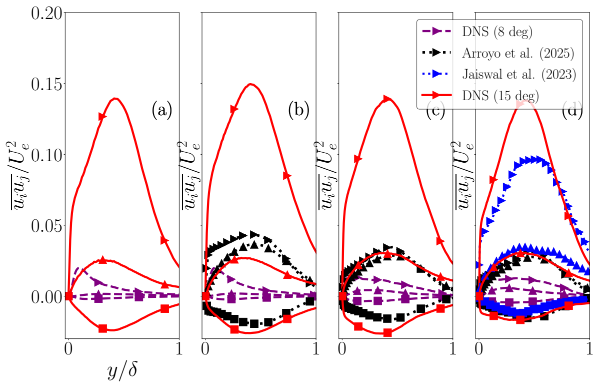

Figure 11. Reynolds stress in the boundary layer at (a) RMP 7, (b) RMP 9, (c) RMP 21, (d) RMP 24. ► $\overline{uu}$, ▲ $\overline{vv}$ and ■ $\overline{uv}$.

than that of (Arroyo Ramo *et al.*, 2026), and this hints at the key role of confinement by the shear layers of the wind tunnel.

3.4 Reynolds stress profiles

Profiles of Reynolds stress inside the boundary layer are shown in Fig. 11. For $\alpha = 15°$, the amplitudes of all Reynolds stress components are stronger and with a maximum peaks shifted away from the wall compared to the attached case at $\alpha = 8°$. At $\alpha = 8°$, the profiles of $\overline{uu}$, $\overline{vv}$ and $\overline{uv}$ remain similar after the mid chord when normalized by outer scales U_e and δ. At $\alpha = 15°$, significant differences in $\overline{uu}$ can be seen at mid-chord (RMP 9) and near the trailing edge (RMP 21 and 24) when comparing the present DNS to the simulation of Arroyo Ramo *et al.* (2026) in which $\overline{uu}$ is much lower than in the present DNS. On the other hand, the results at the trailing edge at RMP 24 show that the peak of the measured $\overline{uu}$ profile of Jaiswal *et al.* (2023) lies between the present DNS and that of Arroyo Ramo *et al.* (2026). This is likely due to differences in confinement. The flapping wind tunnel shear layer plays a role in both the DNS performed in the current study and the experiment of Jaiswal *et al.* (2023) and causes both faster boundary layer growth and more turbulence activity in the outer region as detailed in (Zhou *et al.*, 2025).

4 Anisotropy

According to Pope (2000) and Lumley (1979), it is possible to quantify the anisotropy of the Reynolds stress tensor using the invariants of its deviatoric part normalized by TKE, b_{ij}. This is done though a plot of the second and third invariants, $II = \lambda_1^2 + \lambda_1\lambda_2 + \lambda_2^2$ and $III = -\lambda_1\lambda_2(\lambda_1+\lambda_2) + \lambda_2^2$, which is commonly referred to as the Lumley triangle. The Lumley triangles for the $\alpha = 8°$ and $\alpha = 15°$ cases are shown in Figs 12 and 13 respectively. Each plot shows the variation of anisotropy in the wall normal direction. Boundaries of the triangle represent the limits of realizable turbulence (Lumley, 1979). Each of the 3 vertices of this triangle represent a canonical state of anisotropy. While the bottom vertex represents isotropic turbulence (3C), the top left (2C) and top right vertices (1C) respectively represent axisymmetric two-component and 1-component states, Furthermore, each of the the edges signify types of transition between these canonical states. The edge between (1C) and (3C) represent axisymmetric expanson, the edge between (2C) and (3C) represent axisymmetric contraction while the edge between (1C) and (2C) represent 2-component turbulence. All realizable Reynolds stresses tensors then correspond to points within this triangle (Lumley, 1979).

In the $\alpha = 8°$ configuration, Figs. 12 (a) and (b) show that in the LSB, 2-component turbulence near the wall is followed by axisymmetric contraction. This is followed by a transition to axisymmetric expansion to a point of max anisotropy and then a relaxation towards isotropy away from the wall. This trend matches observations of a separation bubble by Schiavo *et al.* (2017). After the flow reattaches at RMP 5 in Fig 12 (b), a region of 2-component turbulence develops near the wall. This region grows in the ZPG region in Fig 12 (c) and (d), reaching a point of maximum anisotropy before transitioning to axisymmetric expansion and then relaxing toward isotropy further away from the wall. The level of anisotropy, measured by II, reaches higher levels than in the ZPG boundary layer results of Spalart (1988). Furthermore, no full relaxation to isotropic state is seen at the edge of the boundary layer. This matches observations on a NACA0012 ($\alpha = 9°$, $x/c = 0.5$) in (Silva & Wolf, 2024) where II remained at 0.03 at the edge of the boundary layer at the ZPG location . At the APG locations shown in Fig. 12(e,f), the portion of the boundary layer exhibiting two-component turbulence decreases, while the turbulence states shift away from the one-component limit. This behavior is also consistent with the findings of Silva & Wolf (2024).

In the $\alpha = 15°$ configuration, Figs. 12 (a–f) show that the anisotropic state still originates from the two-component axisymmetric limit at the wall for RMP positions 7–24, consistent with the attached-flow behavior observed in the $\alpha = 8°$ case. However, the region of two-component turbulence is reduced, and the transition toward axisymmetric expansion occurs at a smaller wall-normal distance compared to the $\alpha = 8°$

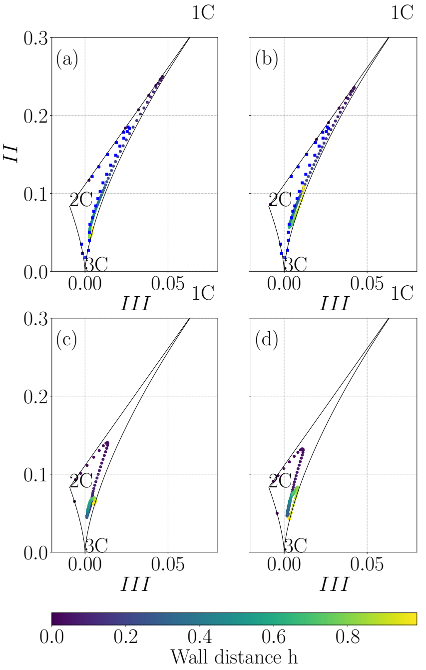

Figure 12. Anisotropy invariant map of $\alpha = 8^\circ$ colored by wall distance.(a) RMP 7,(b) RMP 9,(c) RMP 21,(d) RMP 24 of $\alpha = 8^\circ$. Blue squares represent ZPG results of (Spalart, 1988)

configuration. Above the center of the boundary layer (around h/δ), the axisymmetric expansion state is maintained, consistent with mixing-layer observations reported by (Bell & Mehta, 1990).

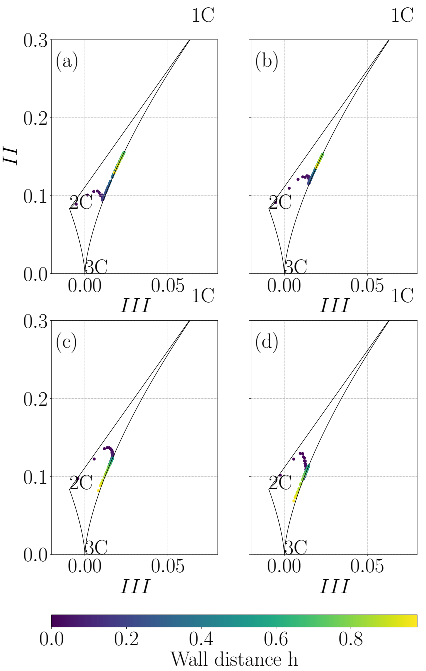

Figure 13. Anisotropy invariant map of $\alpha = 15^\circ$ colored by wall distance.(a) RMP 7,(b) RMP 9,(c) RMP 21,(d) RMP 24. $\alpha = 15^\circ$

4.1 Two-point correlation

Two-point correlations of R_{33} allude to the size and coherence of the turbulence structures in the boundary layer and are relevant for characterizing the integral length scale used in equation 2.

At $\alpha = 8^\circ$, Fig. 14 shows strong streamwise stretching at mid-chord (RMP 7) close to the wall ($x_3 = 0.25\delta$). This result supports observations by Lee & Sung (2011) who reported high streamwise coherence near the wall caused by the presence of hairpin vortices in a turbulent boundary layer at $1410 < Re_\theta < 2560$. Further from the wall, at $x_3 = 0.45\delta$, the spanwise coherence length increases, but the correlation contours remain more stretched in the streamwise than in the spanwise direction. At RMP 24, the contours are less elongated and appear more isotropic compared to those at RMP 7. At both RMP locations, contours in wall-parallel planes indicate homogeneity in the streamwise and spanwise directions, consistent with previous observations by Jaiswal *et al.* (2020).

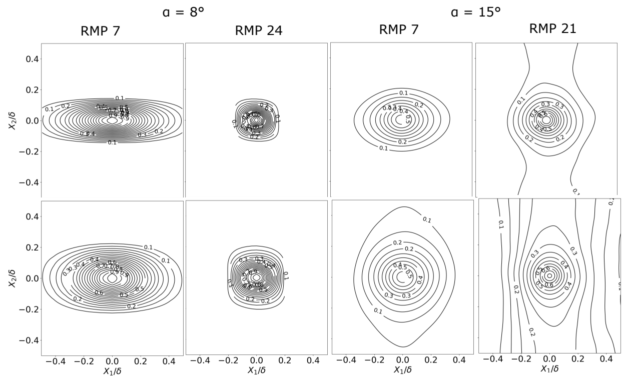

Figure 14. $R_{33}(r_1, r_2, 0)$ at $x_3 = 0.25\delta$ (Top row) and $x_3 = 0.45\delta$ (Bottom row) for $\alpha = 15^\circ$.

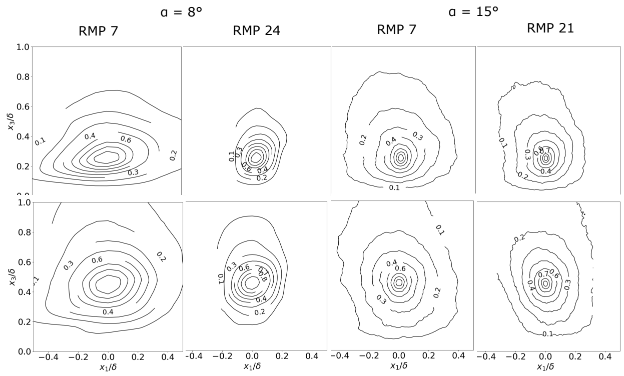

Figure 15. $R_{33}(r_1, 0, r_2)$ at $x_3 = 0.25\delta$ (Top row) and $x_3 = 0.45\delta$ (Bottom row) for $\alpha = 15^\circ$.

At $\alpha = 15^\circ$, $x_3 = 0.45\delta$ coincides with the location of max $|u_1 u_2|$ at RMP 7 and RMP 24. The presence of Kelvin Helmholtz rollers at this peak in $|u_1 u_2|$ (Jaiswal *et al.*, 2023) also cause a strong spanwise coherence which is shown by the significant spanwise stretching of $R_{33}(r_1, r_2, 0)$.

Inhomogeneity due to wall blocking effects (Jaiswal *et al.*, 2020) can be seen in Fig 15 in the wall normal plane for both $\alpha = 8^\circ$ and $\alpha = 15^\circ$ cases at both RMP locations. This is shown by the rapid decrease in correlation near the wall and stretching in the wall normal direction.

4.2 Conclusion

DNS simulations of the CD airfoil installed in an anechoic wind tunnel at $\alpha = 8^\circ$ and $\alpha = 15^\circ$ have successfully achieved and validated with experiments. Mean flow and turbulence statistics of both DNS have been compared. Good collapse of velocity profiles was obtained with embedded shear layer scaling at $\alpha = 15^\circ$. A balance of turbulence kinetic energy (TKE) is performed on the $\alpha = 8^\circ$ case for the first time in a LBM framework, demonstrating sufficient grid resolution for resolving dissipative scales. In terms of anisotropy, the strong near-wall streamwise coherence typical of attached flows is much weaker in the $\alpha = 15^\circ$ case, as seen in both the $\overline{u_1u_1}/\overline{u_2u_2}$ ratio and the streamwise-to-spanwise coherence ratio. Strong spanwise coherence far from the wall at the location of peak $\overline{u_1u_2}$ is present for $\alpha = 15^\circ$ due to the presence of Kelvin-Helmholtz rollers. This shows a need to include spanwise stretching of velocity correlation in models of velocity spectra.

References

Amiet, R 1975 Correction of open jet wind tunnel measurements for shear layer refraction. In *2nd Aeroacoustics Conference*, p. 532.

Arroyo Ramo, Andrea, Moreau, Stéphane, Bauerheim, Michaël & Sandberg, Richard D 2026 Direct noise simulation of an installed controlled diffusion airfoil at high angle-of-attack. *International Journal of Heat and Fluid Flow* p. 110272.

Bell, James H & Mehta, Rabindra D 1990 Development of a two-stream mixing layer from tripped and untripped boundary layers. *AIAA journal* **28** (12), 2034–2042.

Caiazzo, A, Pargal, S, Wu, H, Sanjosé, M, Yuan, J & Moreau, S 2023 On the effect of adverse pressure gradients on wall-pressure statistics in a controlled-diffusion aerofoil turbulent boundary layer. *Journal of Fluid Mechanics* **960**, A17.

Chen, H. 1998 Volumetric formulation of the lattice boltzmann method for fluid dynamics: Basic concept. *Physical Review E* **58** (3), 3955–3963.

Christophe, Julien, Anthoine, Jérome & Moreau, Stéphane 2009 Trailing edge noise of a controlled-diffusion airfoil at moderate and high angle of attack. In *15th AIAA/CEAS Aeroacoustics Conference (30th AIAA Aeroacoustics Conference)*, p. 3196.

Deuse, Mathieu & Sandberg, Richard D 2020 Implementation of a stable high-order overset grid method for high-fidelity simulations. *Computers & Fluids* **211**, 104449.

Devenport, William J & Lowe, K Todd 2022 Equilibrium and non-equilibrium turbulent boundary layers. *Progress in Aerospace Sciences* **131**, 100807.

Grasso, Gabriele, Jaiswal, P, Wu, Hao, Moreau, Stéphane & Roger, Michel 2019 Analytical models of the wall-pressure spectrum under a turbulent boundary layer with adverse pressure gradient. *Journal of Fluid Mechanics* **877**, 1007–1062.

He, X. & Luo, L-S. 1997 Theory of the lattice-boltzmann method: From the boltzmann equation to the lattice boltzmann equation. *Physical Review E* **56** (6), 6811–6817.

Jaiswal, Prateek, Moreau, Stéphane, Avallone, Francesco, Ragni, Daniele & Pröbsting, Stefan 2020 On the use of two-point velocity correlation in wall-pressure models for turbulent flow past a trailing edge under adverse pressure gradient. *Physics of Fluids* **32** (10), 105105.

Jaiswal, Prateek, Rendón, Jose & Moreau, Stéphane 2023 Aeroacoustic investigation of airfoil at near stall conditions. *arXiv preprint arXiv:2307.02109* .

Kraichnan, Robert H 1956 Pressure field within homogeneous anisotropic turbulence. *The Journal of the Acoustical Society of America* **28** (1), 64–72.

Krüger, Timm, Kusumaatmaja, Halim, Kuzmin, Alexandr, Shardt, Orest, Silva, Goncalo & Viggen, Erlend Magnus 2017 The lattice boltzmann method. *Springer International Publishing* **10** (978-3), 4–15.

Lee, Jae Hwa & Sung, Hyung Jin 2011 Very-large-scale motions in a turbulent boundary layer. *Journal of Fluid Mechanics* **673**, 80–120.

Lee, Seongkyu, Ayton, Lorna, Bertagnolio, Franck, Moreau, Stephane, Chong, Tze Pei & Joseph, Phillip 2021 Turbulent boundary layer trailing-edge noise: Theory, computation, experiment, and application. *Progress in Aerospace Sciences* **126**, 100737.

Lumley, John L 1979 Computational modeling of turbulent flows. *Advances in applied mechanics* **18**, 123–176.

Moreau, Stéphane, Henner, Manuel, Iaccarino, Gianluca, Wang, Meng & Roger, Michel 2003 Analysis of flow conditions in freejet experiments for studying airfoil self-noise. *AIAA journal* **41** (10), 1895–1905.

Panton, Ronald L & Linebarger, John H 1974 Wall pressure spectra calculations for equilibrium boundary layers. *Journal of Fluid Mechanics* **65** (2), 261–287.

Pargal, Saurabh 2023 Non-equilibrium wall-bounded turbulence and associated noise generation. PhD thesis, Michigan State University, East Lansing, MI, USA; University of Sherbrooke, QC, Canada.

Pope, Stephen B 2000 *Turbulent flows*. Cambridge university press.

Roger, Michel & Moreau, Stéphane 2005 Back-scattering correction and further extensions of amiet's trailing-edge noise model. part 1: theory. *Journal of Sound and vibration* **286** (3), 477–506.

Sanjosé, Marlène & Moreau, Stéphane 2018 Fast and accurate analytical modeling of broadband noise for a low-speed fan. *The Journal of the Acoustical Society of America* **143** (5), 3103–3113.

Schiavo, Luiz ACA, Wolf, William Roberto & Azevedo, Joao Luiz F 2017 Turbulent kinetic energy budgets in wall bounded flows with pressure gradients and separation. *Physics of fluids* **29** (11).

Silva, Leandro JO & Wolf, William R 2024 Embedded shear layers in turbulent boundary layers of a naca0012 airfoil at high angles of attack. *International Journal of Heat and Fluid Flow* **107**, 109353.

Spalart, Philippe R 1988 Direct simulation of a turbulent boundary layer up to rθ= 1410. *Journal of fluid mechanics* **187**, 61–98.

Wei, Tie & Knopp, Tobias 2023 Outer scaling of the mean momentum equation for turbulent boundary layers under adverse pressure gradient. *Journal of Fluid Mechanics* **958**, A9.

Zhou, Ziyang, Moreau, Stéphane & Sanjosé, Marlène 2025 Direct numerical simulation of installation effects on airfoil noise. *International Journal of Heat and Fluid Flow* p. 110207.

Zhu, Tao, Lallier-Daniels, Dominic, Sanjosé, Marlène, Moreau, Stéphane & Carolus, Thomas 2018 Rotating coherent flow structures as a source for narrowband tip clearance noise from axial fans. *Journal of Sound and Vibration* **417**, 198–215.